Environmental Science & Technology

pubs.acs.org/est

Article

Single-Atom Cobalt Incorporated in a 2D Graphene Oxide Membrane for Catalytic Pollutant Degradation

Xuanhao Wu, Kali Rigby, Dahong Huang, Tayler Hedtke, Xiaoxiong Wang, Myoung Won Chung, Seunghyun Weon, Eli Stavitski, and Jae-Hong Kim*

Cite This: *Environ. Sci. Technol.* 2022, 56, 1341−1351

Read Online

ACCESS | Metrics & More | Article Recommendations | Supporting Information

Downloaded via YALE UNIV on March 12, 2022 at 15:43:18 (UTC).
See https://pubs.acs.org/sharingguidelines for options on how to legitimately share published articles.

ABSTRACT: We introduce a new graphene oxide (GO)-based membrane architecture that hosts cobalt catalysts within its nanoscale pore walls. Such an architecture would not be possible with catalysts in nanoscale, the current benchmark, since they would block the pores or alter the pore structure. Therefore, we developed a new synthesis procedure to load cobalt in an atomically dispersed fashion, the theoretical limit in material downsizing. The use of vitamin C as a mild reducing agent was critical to load Co as dispersed atoms (Co_1), preserving the well-stacked 2D structure of GO layers. With the addition of peroxymonosulfate (PMS), the Co_1-GO membrane efficiently degraded 1,4-dioxane, a small, neutral pollutant that passes through nanopores in single-pass treatment. The observed 1,4-dioxane degradation kinetics were much faster (>640 times) than the kinetics in suspension and the highest among reported persulfate-based 1,4-dioxane destruction. The capability of the membrane to reject large organic molecules alleviated their effects on radical scavenging. Furthermore, the advanced oxidation also mitigated membrane fouling. The findings of this study present a critical advance toward developing catalytic membranes with which two distinctive and complementary processes, membrane filtration and advanced oxidation, can be combined into a single-step treatment.

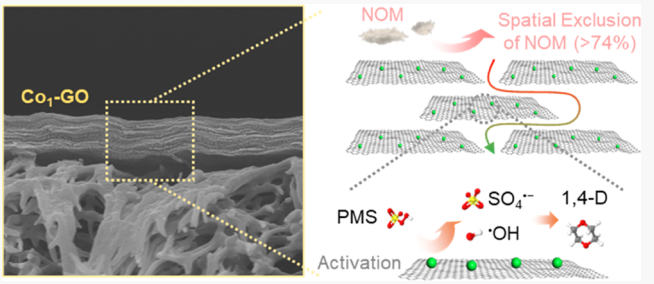

KEYWORDS: *single-atom catalyst, 2D graphene oxide membrane, cobalt, peroxymonosulfate, 1,4-dioxane*

INTRODUCTION

Advancing water treatment membrane materials to gain catalytic properties, in addition to their fundamental function as a passive physical barrier, has been increasingly pursued. The capability to nonselectively destroy organics by highly reactive radicals is particularly appealing toward the goal of reducing membrane fouling by organics and/or destroying pollutants that pass through the membrane pores. Reactive radicals such as $^{\bullet}OH$ and $SO_4^{\bullet-}$ need to be generated *in situ* by activating precursors such as peroxymonosulfate (PMS), peroxydisulfate (PDS), and hydrogen peroxide.[1,2] Employing activation schemes that are established in homogeneous phase advanced oxidation processes (AOPs), such as UV irradiation or the addition of reduced metal ions, is not considered ideal when AOP is coupled with membrane separation. Instead, loading nanocatalysts that enable heterogeneous advanced oxidation onto the membrane surface or inside the pores has been a predominant approach.[3,4]

One challenge in developing catalytic membranes is the disparity in size scale, i.e., membranes that are designed for organic removal have pore sizes in the range of nanometers, e.g., ∼0.5−2 nm (molecular weight cutoff (MWCO) = ∼0.2−1 kDa) for nanofiltration membranes[5] and ∼2−100 nm (MWCO = ∼1−100 kDa) for ultrafiltration membranes.[6] Consequently, nanoparticles in the size range of a few nanometers to tens of nanometers, commonly found in heterogeneous catalytic AOPs, can only be loaded on the surface of the membrane. This is not ideal since the large surface area provided by the pores across the depth of the membrane cannot be utilized for catalytic reactions. Fouling occurs not only on the surface of the membrane but also along the wall of the pores. If the destruction of small organics that pass through the membrane is a target, the catalytic reactions also need to occur as they pass through the pores. However, when nanoparticles are loaded inside the nanosized pores, they can either block the pores and significantly reduce the flux or expand the pore structures to alter their size-exclusion capability. Another inherent limitation of immobilizing nanoparticles includes the leaching of metals or the physical detachment of particles from the support over time.[7]

Received: September 20, 2021
Revised: December 11, 2021
Accepted: December 15, 2021
Published: December 29, 2021

ACS Publications

© 2021 American Chemical Society

This fundamental mismatch provides the motivation for this study. We here aim to load catalysts that derive heterogeneous AOPs onto membrane pores in an atomically dispersed fashion, i.e., single-atom catalysts (SACs). SACs represent the smallest possible material architecture that can be incorporated into pores of nanometer scale without altering the pore structure. SAC exhibits the highest surface-to-volume ratio, thus ensuring that every atom participates in catalytic reactions with close to 100% atomic efficiency,[8] in contrast to nanoparticles in which a large number of metal atoms are buried and wasted under their cluster surface. Strong chemical bonding between a single atom and the substrate provides a more robust anchoring compared to nanoparticles. Many of these benefits have been realized in various catalytic schemes, such as chemical synthesis and fuel production,[9] but have seldom been exploited in the context of developing catalytic membranes.

We target loading cobalt, the metal species most well established as the activator for persulfate, in a single atom configuration (Co_1) onto a graphene oxide (GO)-layered membrane. GO has been widely used as a substrate for various SACs due to its abundant carboxylic, phenolic, and epoxy functional groups that provide anchor sites.[10] In addition, the aromatic π-conjugated network of GO provides abundant delocalized π-electrons for charge transfer in redox reactions.[11] Membranes constructed by layers of GO flakes provide an interlayer distance of typically ~1 nm, serving as an ideal platform to demonstrate SAC loading.[12] However, the current SAC synthesis schemes employing carbonaceous materials (GO,[13−16] carbon nitride (C_3N_4),[17−19] carbon nanotube,[20] zeolitic imidazolate frameworks (ZIFs),[21−23] MXene,[24] and biochar[25,26]) involve high-temperature annealing under N_2 or Ar gas environments. Unfortunately, such treatment removes oxygen functionalities and makes these substrates more hydrophobic. Consequently, the resulting layered structure can suffer from low mechanical stability, crumpling and inhomogeneity in the channel structure, and the loss of the 2D structure of GO, C_3N_4, and MXene layers.[27] Therefore, we developed a new approach to load Co onto GO without severely reducing GO to preserve the intended structural properties of layered GO membranes.

We tested the performance of the Co_1-loaded GO membrane (herein referred to as the Co_1-GO membrane) for the oxidative removal of 1,4-dioxane (1,4-D), a pollutant of considerable concern due to its widespread environmental release and potential toxicity.[28] 1,4-D was the second most prevalent priority contaminant in public water supplies in the U.S.[29] The concentrations of 1,4-D were commonly <1 μg/L in drinking water sites[29] but may reach up to ~100 μg/L in some river and groundwater samples.[30] Due to its small size (molecular weight of 88 g/mol and estimated molecular length and width of 0.71 and 0.66 nm, respectively),[31] hydrophilicity ($\log K_{oc}$ = 1.23), and neutral charge, 1,4-D readily permeates through membranes, even reverse osmosis (RO).[32] We further examine how membrane fouling can be mitigated when the Co_1-GO membrane treats water containing natural organic matter (NOM).

EXPERIMENTAL SECTION

Chemicals and Materials. Graphite flakes, potassium permanganate ($KMnO_4$, 99.0%), 1,4-dioxane ($C_4H_8O_2$, anhydrous, 99.8%), hydrogen peroxide (H_2O_2, solution, 30%), potassium peroxymonosulfate ($KHSO_5{\cdot}0.5KHSO_4{\cdot}0.5K_2SO_4$, OXONE), and L-ascorbic acid ($C_6H_8O_6$, 99%) were purchased from Sigma-Aldrich. Ethanol (C_2H_6O, 100%, 200 Proof) was obtained from Decon Labs. Suwannee River natural organic matter (SRNOM, 2R101N) was obtained from International Humic Substances Society (IHSS). 5,5-Dimethyl-1-pyrroline *N*-oxide (97.0%, DMPO, TCI America) was purchased from Fisher Scientific. Polyethersulfone (PES) membrane (Supor 100, nominal pore size = 0.1 μm, diameter = 25 mm) supports were purchased from PALL. All chemicals used in the experiments were reagent grade or higher and used as received without further purification. Experimental solutions were prepared using deionized water (DI, >18.2 MΩ·cm) from the Milli-Q system.

Synthesis of GO and Co_1-GO Membranes. GO was synthesized based on a previously established method but with several modifications (see Text S1 for details).[33] A Sigma-Aldrich vacuum filtration unit with glass support was used for membrane synthesis. A pristine GO membrane was prepared as a control by filtering suspended GO nanoflakes (0.5 mg/mL, 5 mL, pH adjusted to 6, sonicated for 2 h) through a PES membrane at a GO loading amount of 0.625 mg per PES membrane. To synthesize a Co_1-GO membrane, the same amount of suspended GO nanoflakes (0.5 mg/mL, 5 mL, pH 6) was mixed with cobalt chloride (25 μL from 1 mg Co/mL stock solution), and the mixed suspension was sonicated for 2 h. L-Ascorbic acid (1 mM) was then added into the solution, which was further stirred at 80 °C for 2 h. The color of GO flakes turned from dark brown to black after the chemical reduction. The slightly reduced GO flakes with Co_1 were vacuum filtered onto a PES membrane to form a Co_1-GO membrane. The Co loading amount on the membrane was quantified to be 0.83 wt % (w_{Co}/w_{GO}) using inductively coupled plasma mass spectrometry (ICP-MS). The GO and Co_1-GO membranes were washed using DI water and dried under vacuum conditions for further testing.

Characterizations. The morphology of GO and Co_1-GO flakes suspended in solution was first characterized by transmission electron microscopy (TEM, Tecnai Osiris 200 kV, FEI). ζ-Potentials (ζ, Zetasizer Nano ZS, Malvern Instruments) and dynamic light scattering were measured for the charge and size of GO flakes in aqueous suspension, respectively. The GO and Co_1-GO membranes were characterized by X-ray photoelectron spectroscopy (XPS) with a Versa Probe II scanning XPS microprobe (Physical Electronics) using monochromatic Al Kα radiation (1486.6 eV). The surface and cross-sectional morphology of membranes were examined by scanning electron microscopy (SEM, SU8230 UHR Cold Field Emission, Hitachi). Atomic ratios were quantified by a high spatial resolution X-ray energy-dispersive spectroscopy (EDS) analysis with a BRUKER XFlash 5060FQ annular EDS detector. X-ray diffraction (XRD, Rigaku SmartLab) using Cu Kα radiation (λ = 1.542 Å) was conducted to characterize the *d*-spacing of GO flakes in the membrane. Raman spectroscopy (LabRAM HR Evolution, Horiba) was carried out to observe the characteristic D and G bands of GO. Attenuated total reflection Fourier transform infrared spectroscopy (ATR-FTIR, IRTracer-100, Shimadzu) was used to characterize oxygen-containing functional groups. The pore size and MWCO of the membranes were measured by evaluating the rejection of poly(ethylene glycol)s (PEG) with varying molecular weights (see details in the SI, Text S2).[34]

https://doi.org/10.1021/acs.est.1c06371
Environ. Sci. Technol. 2022, 56, 1341−1351

To characterize Co SAs, X-ray absorption spectra (XAS) at Co K-edge were conducted at Beamline 8-ID of the National Synchrotron Light Source II at Brookhaven National Laboratory, using a Si(111) double-crystal monochromator and a passivated implanted planar silicon (PIPS) fluorescence detector. Near-edge X-ray absorption spectroscopy (XANES) data were collected at room temperature, with energy calibrated using a Co foil. The morphology of Co SAs was measured using high-angle annular dark-field scanning transmission electron microscopy (HAADF-STEM) with a JEM-2100F (JEOL) instrument operated at 200 kV, coupled with Cs correction. Lacey carbon/300 mesh Cu grid was used for the STEM elemental mapping of the catalyst.

Pollutant Removal Tests. The performance of the GO and Co_1-GO membranes for PMS activation and 1,4-D treatment was tested in a dead-end flow-through system. The feed solution was prepared by dissolving 50 mg/L 1,4-D and PMS (1 or 3 mM). The initial pH of this mixed solution was 3.5, and it was increased using sodium hydroxide (1 M) to 6.0 and 9.5 to evaluate pH effects. The pressure was set at 30 psi (~2 bar) using N_2 gas. The membrane permeate samples were analyzed using an Agilent high-performance liquid chromatograph (HPLC, Agilent Technologies 1260 Infinity), equipped with a C18 column (4.6 mm × 250 mm, 5 μm). The mobile phases were set as 10 (v/v)% acetonitrile and 90 (v/v)% phosphoric acid (0.1 (v/v)%), with 1 mL/min flow rate, absorption at 200 nm, and 2.36 min retention time. PMS concentrations were measured using a spectrophotometric method based on iodometric titration.[35] Total organic carbon (TOC) concentration was measured using a Shimadzu TOC analyzer. Electron paramagnetic resonance (EPR) analyses were conducted with the ESR-300E spectrometer (Bruker Instruments) using DMPO (120 mM) as the spin-trapping agent for $SO_4^{\bullet-}$ and $^{\bullet}OH$.

RESULTS AND DISCUSSION

Characterization of Atomically Dispersed Co. The synthesis procedure we newly developed in this study is schematically illustrated in Figure 1. We first electrostatically

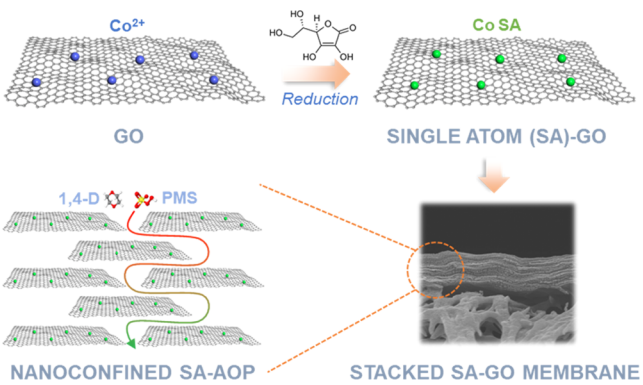

Figure 1. Schematic showing the synthesis of the Co_1-GO layered membrane for flow-through catalytic pollutant removal.

anchored Co^{2+} to the surface of GO flakes suspended in water at pH 6. ζ-Potential measurements confirmed that GO flakes were negatively charged within the pH range 1−9 (Figure S1a). The ζ-potential increased from −33.3 ± 1.8 to −28.2 ± 2.2 mV after the addition of Co^{2+}, indicating the binding of Co^{2+} ions onto the GO flakes. We then applied vitamin C (VC; L-ascorbic acid) as a mild reducing agent to reduce Co^{2+} to Co single atoms (Co_1-GO). We observed that the hydrodynamic particle size decreased slightly from ~400 to ~340 nm, presumably due to the vigorous mixing we applied during reduction (Figure S1b). However, the 2D structure of GO flakes was preserved according to TEM analysis (Figure S1c,d). TEM elemental mapping confirmed the uniform distribution of Co, C, and O atoms across the Co_1-GO surface (Figure S1e). The emergence of XPS peaks for Co 2p further confirmed the successful loading of Co_1 with the oxidation state close to +2 (Figure S2a). XPS C 1s analysis suggested that GO was also slightly reduced during VC application, as evidenced by a higher percentage of C−C bonds (42%) and lower percentages of C−O (50%) and C═O (8%) bonds in Co_1-GO compared to GO (Figure S2b).

HAADF-STEM characterization provided visual evidence for the presence of atomically dispersed Co_1 on GO flakes (Figure 2b). We did not observe any cluster bigger than bright dots on an Å scale, excluding the formation of nanoparticles. The lack of metal clusters was further confirmed by the Co K-edge XANES spectra, in which the white-line intensity of Co_1-GO was drastically different from metallic Co (i.e., Co foil). Instead, the peak was very close to that of the CoO reference (Figure 2c).[36] This result suggests that Co_1 is positively charged at approximately +2, consistent with XPS results. The result of Fourier-transformed extended X-ray absorption fine structure (FT-EXAFS) analysis showed that the first coordination shell of Co_1 was located at 1.56 Å (Figure 2d), close to the Co−O interaction in the CoO reference (1.59 Å). However, the Co−Co interaction in CoO (nearest shell, 2.58 Å) was almost absent in Co_1-GO, indicating the absence of cobalt oxide.[37,38] Consequently, we conclude that Co atoms are coordinated with oxygen atoms of GO.[39] This binding environment of Co_1 on GO was similar to previously reported Co_1-GO flakes synthesized using the high-temperature annealing method.[36] The lack of a peak at a radial distance of 2.21 Å, representing the Co−Co coordination from the Co foil reference,[36] suggests the absence of metallic nanoclusters/nanoparticles and the isolation of Co as dispersed single atoms. Further fitting of the FT-EXAFS spectra showed an averaged Co−O coordination number of ~2.3 with a Co−O radial distance at 2.12 Å (Figure 2e and Table S1), indicating that Co_1 was bound to two oxygen atoms in the carboxyl, hydroxyl, or epoxy groups of GO.

Characterization of GO and Co_1-GO Membranes. We filtered the above-prepared GO and Co_1-GO flakes through supporting PES membranes to deposit GO and Co_1-GO flakes in a layered fashion to prepare GO-layered membranes. It is important to note that the GO layers were also mildly reduced during the Co reduction step. Consequently, we observed that the water contact angle increased from 32 ± 1° for the GO membrane (Figure 3a inset) to 45 ± 1° for the Co_1-GO membrane (Figure 3b inset). We confirmed the changes in surface functionality via ATR-FTIR (Figure 3c). For the GO membrane, we observed peaks at 1625 cm^{-1} (aromatic C═C and conjugated carbonyl C═O), 1730 cm^{-1} (carboxyl and ketonic carbonyl stretching), and ~3400 cm^{-1} (−OH mainly from phenolic or carboxylic groups since the membranes were fully dried under vacuum conditions to exclude adsorbed H_2O).[40−42] After reacting with VC, the intensities of 1625 and 3400 cm^{-1} peaks decreased, while the intensity of the 1730 cm^{-1} peak remained similar. These results suggest that the mild reduction leads to the loss of aromatic C═C, conjugated

https://doi.org/10.1021/acs.est.1c06371
Environ. Sci. Technol. 2022, 56, 1341−1351

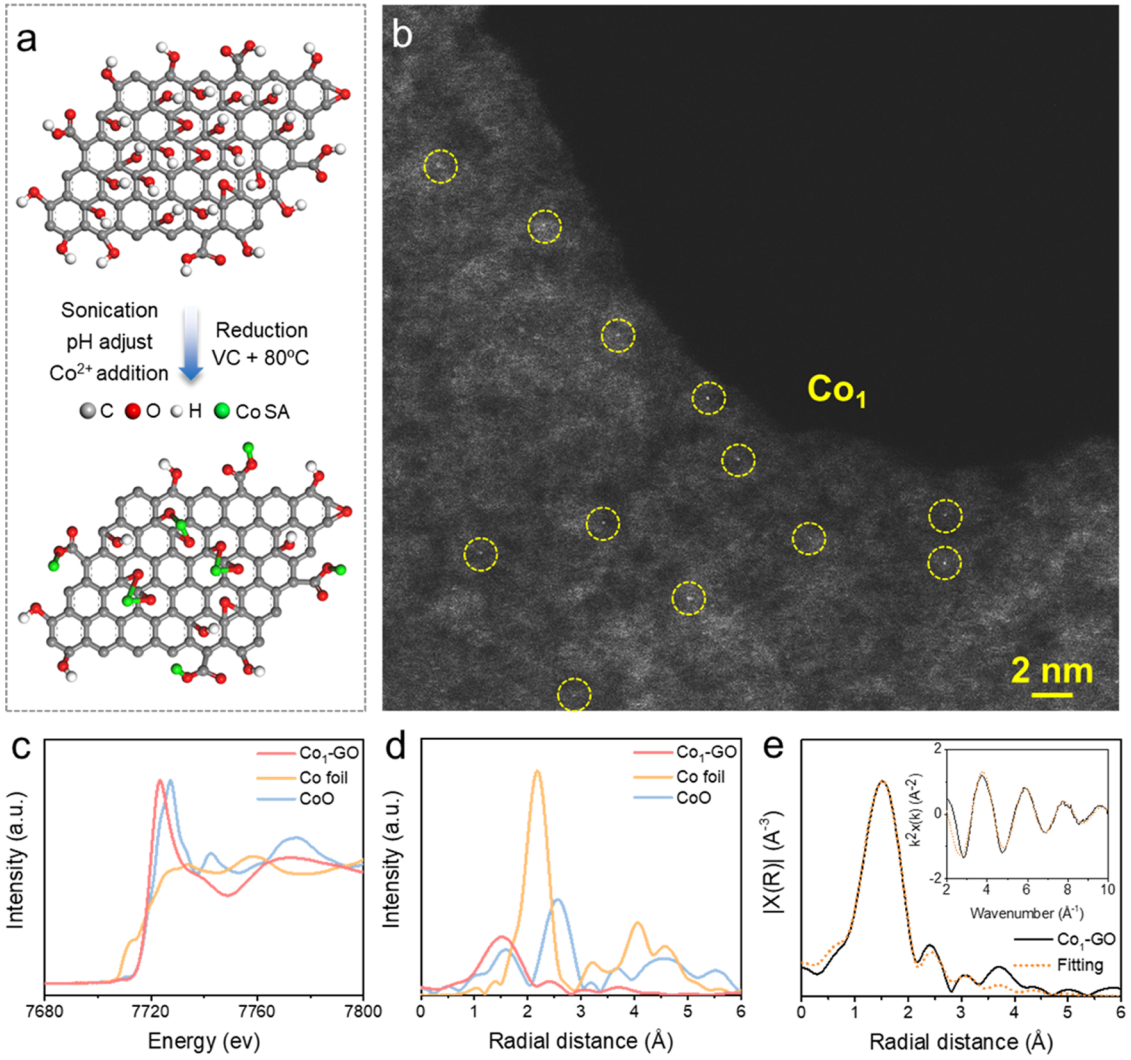

Figure 2. (a) Schematic showing the synthetic procedures of Co_1-GO. (b) HAADF-STEM image of Co SAs on the GO nanoflakes. (c) XANES spectra of the Co_1-GO membrane, Co−Co (Co foil reference), and Co−O (CoO reference). (d) FT-EXAFS spectra of the Co_1-GO membrane, Co−Co (Co foil reference), and Co−O (CoO reference). (e) Fitting of the Co_1-GO membrane FT-EXAFS spectrum (inset: fitting of corresponding *K*-space spectrum).

carbonyl C═O, and hydroxyl groups after reduction. The loss of −OH was consistent with the increased hydrophobicity of the membrane as revealed from contact angle measurements.

While both membranes exhibited similar surface morphologies (Figure 3a,b) and ordered, layered cross-sectional 2D structures (Figure 3d,e), we also observed that the thickness of GO layers decreased from 720 ± 50 nm for the GO membrane to 550 ± 40 nm for the Co_1-GO membrane, despite the fact that we loaded the same mass of samples onto the PES support. Consistently, GO layers of the Co_1-GO membrane had an interlayer spacing of 7.31 Å (2θ = 12.1°), which was smaller than 7.69 Å (2θ = 11.5°) of the GO membrane according to XRD analysis (Figure 3f). The decrease in the interlayer spacing of GO flakes and the overall membrane thickness after reduction are mainly ascribed to the removal of out-of-plane oxygen-containing functional groups and the subsequent increase in hydrophobic interactions between adjacent layers.[43] This is also consistent with past observations for the layers of GO reduced by thermal treatment[44] or chemical reducing agents including VC.[43,45,46] The XRD pattern of a GO membrane treated with only VC (GO-VC, without Co_1) also showed a similar shift of the 2θ peak compared to the Co_1-GO membrane, suggesting that this alteration of lattice distance mainly resulted from the reduction of GO instead of from Co_1 intercalation, as we have intended with the use of Co_1. The absence of XRD peaks from cobalt nanoparticles (2θ = 45°)[47] or cobalt oxides (2θ = 34 and 42° for CoO and 2θ = 32, 36, and 44° for Co_3O_4)[48] further excluded the formation of these phases.

***In Situ* 1,4-Dioxane Removal via PMS Activation.** We evaluated the performance of GO and Co_1-GO membranes using a dead-end filtration cell (Figure 4a). The rejection of 10 kDa PEG was comparable between the two: 99% by the GO membrane and 97% by the Co_1-GO membrane (Figure S5). This indicates that both membranes had similar MWCO corresponding to effective pore sizes in the range of 3−5 nm (Text S2 for calculation), close to commercial ultrafiltration membranes.[6] The pore size determined by PEG appears larger than the interlayer spacing measured by XRD due to the swelling of GO layers in water.[49] Water fluxes under 30 psi were also comparable at 1.9 ± 0.4 and 2.1 ± 0.4 L/m^2·h (Figure 4b) for the GO and the Co_1-GO membranes,

https://doi.org/10.1021/acs.est.1c06371
Environ. Sci. Technol. 2022, 56, 1341−1351

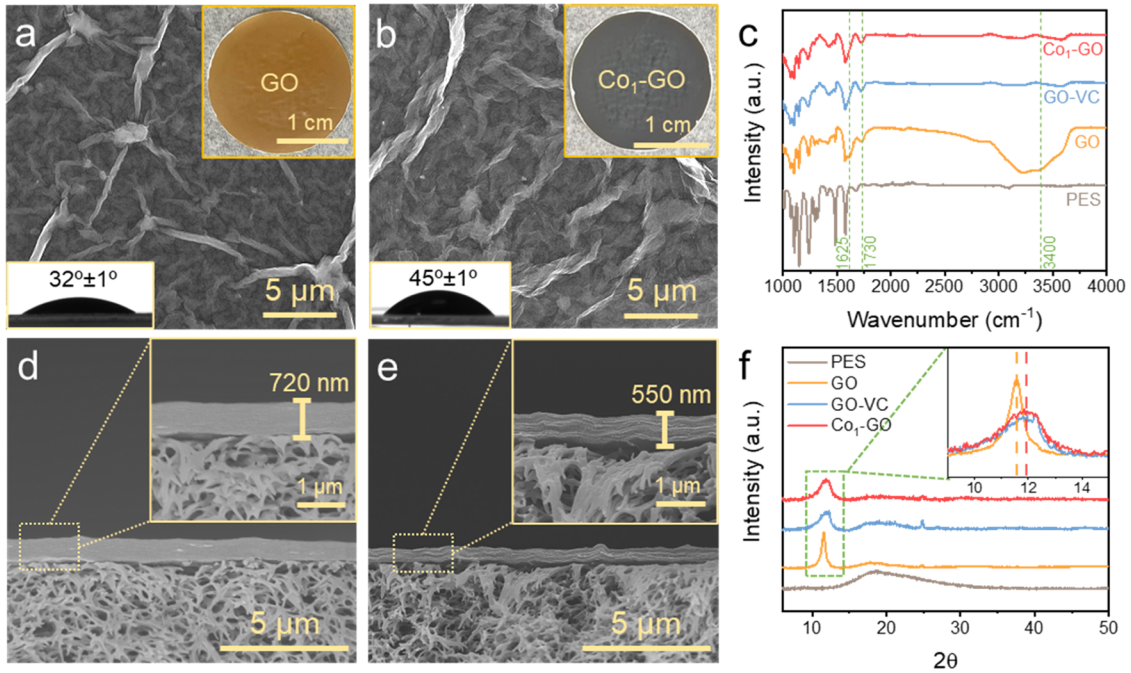

Figure 3. Surface SEM images of (a) the pristine GO membrane and (b) the Co_1-GO membrane. Insets: optical images and contact angles of two membranes. (c) ATR-FTIR spectra of the PES, GO, GO-VC, and Co_1-GO membranes. Cross-sectional SEM images of (d) the pristine GO membrane and (e) the Co_1-GO membrane. (f) XRD patterns of the PES, the pristine GO, the GO-VC, and the Co_1-GO membranes.

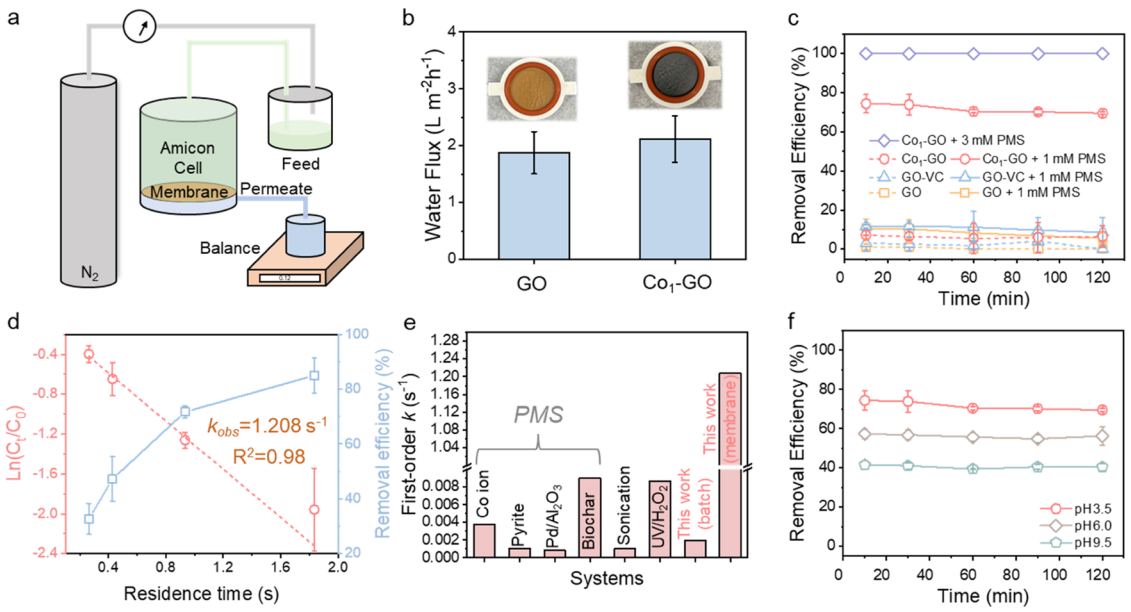

Figure 4. (a) Schematic illustrating the flow-through testing system. (b) Water fluxes of the GO and the Co_1-GO membranes (50 mg/L 1,4-D, 1 mM PMS, pH 3.5, 30 psi pressure). (c) 1,4-D removal efficiencies of the GO, the GO-VC, and the Co_1-GO membranes within 2 h. (d) First-order kinetic rate constant k_{obs} determined by linear regression of $\ln([C]_t/[C]_0)$ (left *y*-axis) versus residence time *t* (s). Right *y*-axis: removal efficiencies of 1,4-D by the Co_1-GO membrane at different residence times. (e) Comparison of first-order rate constants *k* from this work (1 mM PMS and pH 3.5) in the batch system and membrane system with previous studies. The rate constants for 1,4-D degradation reported in these studies are within the same order of magnitude as the batch system in our study and therefore served as comparison benchmarks. (f) Removal efficiencies of 1,4-D of the Co_1-GO membrane under three pH conditions. For all figures, error bars are calculated from triplicate tests.

respectively. This result suggests that the pore size of water channels across the layered GO membrane did not alter much by the loading of Co_1 at approximately 1 wt % (quantified by both EDS analysis (Figure S4) and ICP-MS). A slightly lower PEG rejection and slightly higher water permeation with the Co_1-GO membrane, despite denser layers of GO flakes, are believed to have resulted from smaller sizes of GO flakes (i.e., due to intense agitation during GO reduction) and the reduction in overall flow path length.[50]

In marked contrast, the catalytic performance of the Co_1-GO membrane was significantly better than the GO membrane when filtering water containing 50 mg/L 1,4-D and 1 mM PMS at pH 3.5. The Co_1-GO membrane removed 71.7% of 1,4-D, while the GO membrane only removed 8.3% (Figure

https://doi.org/10.1021/acs.est.1c06371
Environ. Sci. Technol. 2022, 56, 1341−1351

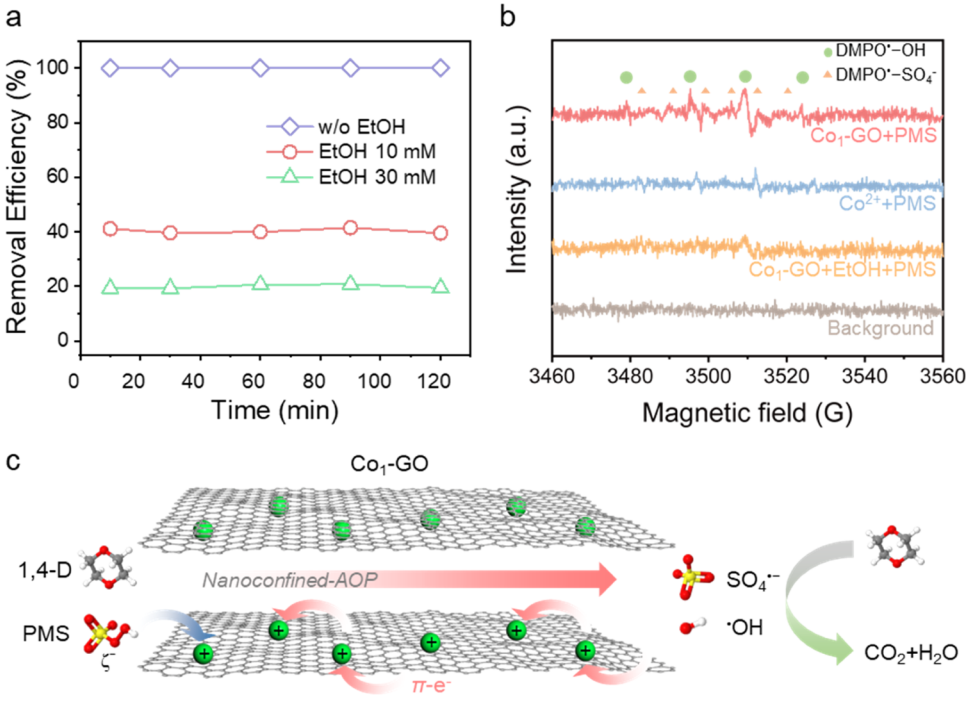

Figure 5. (a) Removal efficiencies of 1,4-D with and without EtOH (50 mg/L 1,4-D, 3 mM PMS, pH 3.5, 30 psi pressure). (b) EPR spectra of systems using DMPO (120 mM) as the spin-trapping agent. (c) Proposed degradation mechanisms of 1,4-D in the Co_1-GO membrane during the flow-through PMS activation.

4c). When PMS concentration was increased to 3 mM, the Co_1-GO membrane achieved a 100% removal rate of 1,4-D. We ascribed the 1,4-D removal mostly to catalytic destruction since both GO and Co_1-GO membranes did not remove 1,4-D over 2 h of filtration either by size exclusion or adsorption in the absence of PMS. PMS concentration in the permeate of the Co_1-GO membrane under 1 mM PMS decreased to 0.68 mM, indicating the successful activation of PMS by Co SAs (Figure S7). The efficiency of the GO membrane to activate PMS was minimal, consistent with previous studies showing negligible PMS activation by GO.[51] While it is known that reduced GO more efficiently activates PMS,[52] we also observed that the membrane made with GO after VC treatment (without Co_1 loading) marginally increased 1,4-D removal to 10.6%. This result alternatively indicates that VC reduction is mild and the resulting GO is different from reduced GO that is typically prepared by more intense reduction schemes, such as thermal annealing or the use of strong reductants such as $NaBH_4$.[53]

Note that for the Co_1-GO membrane with a flux of 2.1 ± 0.4 $L/m^2{\cdot}h$ and 3 mM PMS, a near complete destruction of 1,4-D was achieved within 0.9 s, the residence time of water inside the pores of membranes. We further quantified the rate constant of 1,4-D degradation within the Co_1-GO membrane by varying the pressure and water flux with 1 mM PMS. Increasing the water flux corresponds to decreasing the residence time inside the membrane pores, similar to changing the reaction time in batch systems (Figure 4d). After a linear regression of $\ln([C]_t/[C]_0)$ versus t, the first-order rate constant k was determined to be 1.208 s^{-1} (corresponds to a half-life of 0.57 s), which was ~635 times higher than that in the batch suspension system (1.9×10^{-3} s^{-1} at 1 mM PMS and pH 3.5), and ~130−1500 times higher than previously reported rate constants of 1,4-D degradation by Co^{2+} ion,[54] pyrite,[55] Pd/Al_2O_3,[56] and biochar[57] catalyzed PMS AOPs, as well as sonication[58] and UV/H_2O_2[59] (Figure 4e).

Increasing the feedwater pH negatively affected the performance of the Co_1-GO membrane (Figure 4f). As pH increased from 3.5 to 6.0 and 9.5, the removal rates decreased from 71.7 to 56.2 and 40.6%, respectively. The decreased removal rates of 1,4-D at higher pH values when using PMS as the peroxide precursor were consistent with previous studies.[56,57,60] Within this pH range (3.5−9.5), GO flakes were negatively charged and their surface charge did not vary significantly with pH (Figure S1a). Therefore, the surface charge effects on PMS adsorption might not be significant. Other mechanisms likely contribute to the lower degradation efficiencies at higher pH values, such as an increased quenching of $SO_4^{\bullet-}$ to shorter-lived and less reactive $^{\bullet}OH$ by OH^-,[61] and a greater fraction of less reactive SO_5^{2-} ($E^0(SO_5^{2-}/SO_4^{2-})$ = 1.22 V) than HSO_5^- ($E^0(HSO_5^-/SO_4^{2-})$ = 1.75 V) since PMS has a pK_{a2} value of 9.3.[57,62,63]

The Co_1-GO membrane maintained its initial physical and catalytic properties over long-term operation (48 h of continuous filtration). With the addition of 3 mM PMS at pH 3.5, the Co_1-GO membrane continued to achieve 100% removal of 1,4-D at 30 psi (Figure S8a). The membrane did not show any discernible disintegration upon visual inspection (Figure S8b), and its hydrophilicity remained constant (Figure S8b) and microscopic morphology was preserved (Figure S8c). XRD observations (Figure S8d) suggested that the lattice spacing of the GO layers did not change after dried again in air. We also did not observe GO oxidation in XPS analysis (Figure S8e) despite being exposed to a strongly oxidative environment. FT-EXAFS (Figure S8f) and XANES (Figure S8g) analyses confirmed that Co remained as single atoms instead of aggregating into nanoparticles and the oxidation state of Co_1 did not change. Finally, we found that the release of Co ions from the membrane was minimal (Figure S8h) and the Co concentrations in the permeate remained below the U.S. EPA reclaimed water limit (50 μg/L).[64] Note that the accumulated

https://doi.org/10.1021/acs.est.1c06371
Environ. Sci. Technol. 2022, 56, 1341−1351

Co release after 48 h accounted for only 3% of the entire Co in the membrane, suggesting the high stability of Co_1 anchored on the GO flakes.

Mechanistic Insights. Consistent with the PMS activation by the Co_1-GO membrane discussed above, we observed that a majority of 1,4-D was degraded by *in situ* generated radicals. With the addition of 10 and 30 mM ethanol, a quencher for both $SO_4^{\bullet-}$ and $^{\bullet}OH$ (second-order rate constants = $1.6-7.7 \times 10^7$ and $1.2-2.8 \times 10^9$ M^{-1} s^{-1},[65,66] respectively), to the feed containing 3 mM PMS and pH 3.5, the removal efficiencies of 1,4-D dropped from 100 to 40.4 and 19.9%, respectively (Figure 5a). This result confirmed the major contributions of $SO_4^{\bullet-}$ and $^{\bullet}OH$ to 1,4-D degradation in PMS activation, which was further supported by the EPR measurement using DMPO (120 mM) as the spin-trapping agent in a suspension system, where Co_1-GO flakes were mixed with PMS (Figure 5b). We observed the characteristic peaks of DMPO$^{\bullet}$−OH and DMPO$^{\bullet}$−SO_4^-[67,68] at similar intensities with previous heterogeneous cobalt catalysts for PMS activations.[62,67,69] The peak intensities were also higher than those in the Co^{2+} + PMS system, suggesting higher reactivities of Co single atoms on GO than homogeneous Co ions. The primary contribution of $SO_4^{\bullet-}$ and $^{\bullet}OH$ is consistent with the past reports using Co^{2+} or peroxone to activate persulfate for 1,4-D degradation[54,70] and has also been verified by studies using Co_1 on carbon supports for decomposing other organic pollutants.[14,18,64,71] The contribution of other reactive oxygen species such as $O_2^{\bullet-}$ is likely negligible due to its low oxidation potential ($E^0(O_2^{\bullet-}/O_2) = -0.33$ V) and rapid transformation.[72,73] A nonradical pathway such as electron transfer from 1,4-D to PMS could also have played a minor role in Co_1-PMS systems.[24,71,74]

We attribute the efficient PMS activation and the fast 1,4-D degradation kinetics of the Co_1-GO membrane to the following reasons (Figure 5c). First, Co_1 on GO is positively charged due to the coordination of the electropositive Co atoms (electronegativity = 1.88) with the electronegative O atoms (electronegativity = 3.44), which was observed from XPS and XANES measurements. In contrast to negatively charged GO flakes, the positive charge of Co SAs likely facilitates the adsorption of negatively charged PMS ions. Second, the aromatic π-conjugated network of GO provides abundant delocalized π-electrons,[11] which can transfer to adsorbed PMS molecules through the Co atoms, and then facilitates the cleavage of the O−O bond of PMS and may also stabilize the surface-bound $SO_4^{\bullet-}$ or $^{\bullet}OH$.[75] Third, the pore size range of the Co_1-GO membrane (3−5 nm) is far less than the critical size (~25 nm) that triggers the nanoconfinement effect of surface-catalyzed reactions,[2,76] thus enhancing the contact between short-lived reactive radicals with the target molecule 1,4-D inside the nanosized water channels. Last, compared to previous batch systems where catalysts were suspended and may agglomerate, the flow-through system promotes a contact between the pollutant and the catalyst surface, thus facilitating surface catalysis.[77]

Alleviation of the Organic Matter Effect by Spatial Separation. Membrane filtration and AOP are complementary to each other. AOP needs to be preceded by pretreatment, often membrane filtration,[78] to remove particulate and dissolved matter, including NOM (0.1−20 mg/L).[79] Otherwise, NOM can consume reactive radicals (e.g., $k_{^{\bullet}OH/NOM} \approx 10^9$ M^{-1} s^{-1},[80] $k_{SO_4^{\bullet-}/NOM} \approx 10^8$ M^{-1} s^{-1}[81]) to significantly reduce AOP efficiency. The reaction of NOM with radicals can also lead to the generation of toxic disinfection byproducts when chloride ions are present.[82] Membrane processes, even RO, fail to remove small, neutral organics such as 1,4-D, requiring post-treatment to destroy them. Therefore, designing a filtration membrane with tight pore sizes and catalytic properties combines these two disparate processes into a single-step treatment, i.e., size-exclusion separation of larger organics by the membrane and oxidative destruction of small organics that pass through the membrane. In addition, since oxidation occurs throughout the pores, the removal of organics that contribute to the fouling of the pore surface can be an additional benefit of combining these two processes.

We first demonstrate that the Co_1-GO membrane can significantly decrease the NOM scavenging effects by spatially separating NOM from 1,4-D. We first confirmed the scavenging effects of NOM on 1,4-D removal by Co_1-GO flakes in a batch suspension system (Figure 6a). In the presence of NOM (10 mg/L, ~2 mg C/L confirmed by TOC measurement), the degradation of 1,4-D by suspended Co_1-GO flakes at 2 min decreased from 36 to 23% with 1 mM PMS and from 65 to 57% with 3 mM PMS. In stark contrast, 1,4-D removal through the Co_1-GO membrane was largely prevented with the same feed (Figure 6b). For instance, the removal efficiencies only decreased from 71.7 to 67.3% with 1 mM PMS and from 100 to 94.5% with 3 mM PMS in the presence of NOM.

The Co_1-GO membrane, without catalytic reaction, was able to remove 74% of NOM based on TOC by just size exclusion (Figure S10a). NOM is generally considered to mainly contain acids with MWs less than 10 kDa,[83] including small-MW fulvic acid (<2 kDa) and high-MW humic acid (1−8 kDa).[84] The MWs of NOM compositions, especially humic acids, are close to the MWCO determined for the Co_1-GO membrane (4.15−10 kDa, Figure S5), accounting for the extent of size exclusion we observed. When we added PMS at 1 and 3 mM, the Co_1-GO membrane removed 91 and 98% of NOM, respectively, via both size exclusion at the membrane surface and oxidation along the membrane pores. Considering that 1,4-D and other pollutants are often found in trace concentrations, the results suggest that the Co_1-GO membrane can be used to remove a majority of organics including small MW-NOM and trace organics such as 1,4-D.

We also observed the Co_1-GO alleviated membrane fouling via catalytic oxidation of organic foulants. The average flux of organic-free water through the Co_1-GO membrane within 2 h was 2.1 ± 0.4 L/m^2·h under 30 psi. This flux dropped to 1.8 ± 0.3 L/m^2·h when the feed contained only 10 mg/L NOM (i.e., no PMS) (Figures 6c and S10b). Accordingly, we observed that the contact angle of the Co_1-GO membrane increased from initial 45 ± 1 to $53 \pm 1°$ after filtering NOM-containing water (Figure S10c). This is due to the adsorption of hydrophobic fractions of NOM onto the GO.[85] In contrast, the water flux over 2 h when filtered water contained 10 mg/L NOM and PMS at 1 or 3 mM was the same as the organic-free water filtration flux. We in fact observed that the contact angles of the membrane surface dropped back to 46 ± 2 and $43 \pm 2°$, respectively (Figure S10d,e), indicating that the hydrophobic organic matter adsorbed on the membrane was decomposed.

The performance of the Co_1-GO membrane in a more realistic condition was further evaluated using simulated surface water based on the method developed by the Nanotechnology-Enabled Water Treatment (NEWT) Center

https://doi.org/10.1021/acs.est.1c06371
Environ. Sci. Technol. 2022, 56, 1341−1351

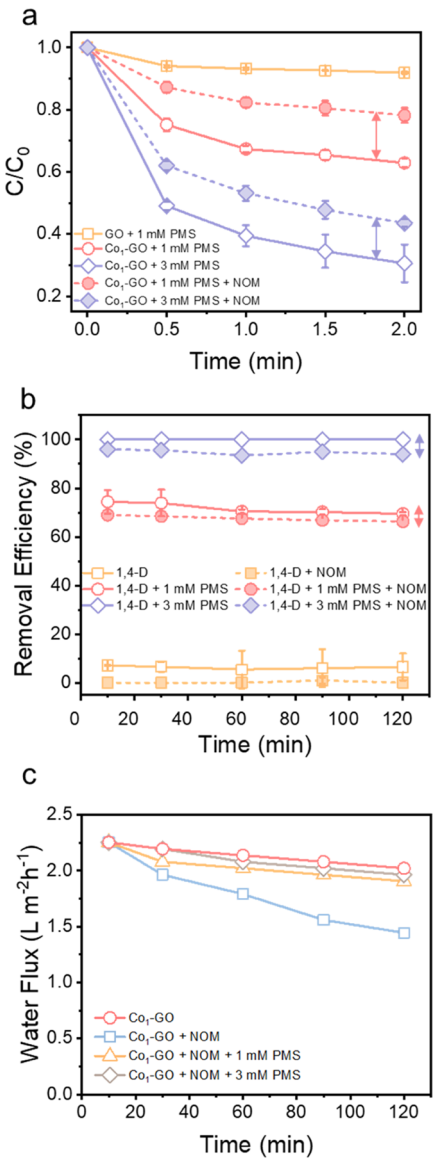

Figure 6. (a) Degradation of 1,4-D in the batch systems with suspended Co_1-GO flakes (0.03 mg/mL), 1,4-D (50 mg/L), PMS (1 and 3 mM), and NOM (10 mg/L). (b) Removal efficiencies of 1,4-D by the Co_1-GO membrane in flow-through systems with and without NOM (10 mg/L). Error bars were from triplicate tests. (c) Water flux variations of the Co_1-GO membrane within 2 h without NOM and with NOM plus 0, 1, and 3 mM PMS (all at pH 3.5, 30 psi pressure).

(Table S2) spiked with 1,4-D, PMS, and NOM. The presence of NOM did not affect the 1,4-D degradation kinetics in the simulated surface water (Figure S11). However, we observed a decrease in removal efficiencies when comparing the NEWT test water results with DI water results under similar conditions (Figures 4c,f and 6b). This performance reduction in the simulated surface water is likely to have resulted from the following: (i) the initial pH of the simulated water was around 7.5 and further tuned to 7.0 when spiked with 1 mM PMS, which was still higher than the pH 3.5 used in DI water condition. This higher pH can lead to lower 1,4-D degradation as verified by pH effect tests (Figure 4f). (ii) The chloride and bicarbonate anions in the NEWT test water may scavenge $SO_4^{\bullet-}$ or $^{\bullet}OH$ to form less reactive radicals including $Cl_2^{\bullet-}$ ($E^0(Cl_2^{\bullet-}/Cl^-)$ = 2.09 V) and $CO_3^{\bullet-}$ ($E^0(CO_3^{\bullet-}/CO_3^{2-})$ = 1.57 V),[86] thus decreasing the overall 1,4-D degradation.[54,56] Note that this decrease of removal efficiencies can be compensated by increasing PMS concentrations (e.g., from 1 to 3 mM PMS).

ENVIRONMENTAL IMPLICATIONS

The findings of our study mark an important advance in a membrane material design toward the development of catalytic membranes. By downsizing the catalyst dimension below the nanoscale and to the single atom limit, we successfully loaded Co catalysts onto a layered GO membrane without altering its size exclusion and water permeation properties. The use of a mild reducing agent, VC, for Co_1 deposition during the synthesis was critical to preserve the physical properties of GO membranes (i.e., the hydrophilicity, well-aligned 2D layered structure, nanosized water channels, and mechanical robustness under the high-pressure filtration process), which were difficult to achieve when using the conventional high-temperature annealing method. Such a design, as demonstrated in this study for the catalytic removal of 1,4-D, has the potential to introduce various catalytic functionalities to water treatment membranes, where the permeation of low-molecular-weight, neutral pollutants present a significant concern and limit membrane process applications. Alternatively speaking, pollutant degradation is efficiently achieved inside the pores, since a large fraction of NOM is size-excluded at the pore entrance. In addition, this design also provides an innovative strategy to enhance the long-term filtration performance by catalytically degrading organics that foul the membrane surfaces and pores, especially for membranes with nanosized pores (e.g., UF and NF). We believe that the material presented in this study is one example among many catalyst-membrane combinations that can be further pursued. In particular, we expect that loading Fenton-like catalysts in SAC configuration onto various high-pressure, nanoporous membranes made of materials that are resistant to oxidation presents a great opportunity to realize the strategy to combine membrane filtration and AOP.

ASSOCIATED CONTENT

Supporting Information

The Supporting Information is available free of charge at https://pubs.acs.org/doi/10.1021/acs.est.1c06371.

Graphene oxide synthesis; PEG rejection method and calculations; XAFS data fitting; ζ-potentials; hydrodynamic particle sizes; TEM; STEM elemental mapping; XPS and SEM images of a PES membrane support; SEM-EDS; PEG rejection; XRD, Raman, PMS concentrations, long-term stability of the Co_1-GO membrane; DMPO mechanism; TOC; contact angles; NEWT water tests; and BPA tests (PDF)

AUTHOR INFORMATION

Corresponding Author

Jae-Hong Kim − *Department of Chemical and Environmental Engineering, Yale University, New Haven, Connecticut 06511, United States;* orcid.org/0000-0003-2224-3516; Phone: +1-203-432-4386; Email: jaehong.kim@yale.edu; Fax: +1-203-432-4387

https://doi.org/10.1021/acs.est.1c06371
Environ. Sci. Technol. 2022, 56, 1341−1351

Authors

Xuanhao Wu − *Department of Chemical and Environmental Engineering, Yale University, New Haven, Connecticut 06511, United States;* orcid.org/0000-0001-6177-6089

Kali Rigby − *Department of Chemical and Environmental Engineering, Yale University, New Haven, Connecticut 06511, United States;* orcid.org/0000-0002-4582-2388

Dahong Huang − *Department of Chemical and Environmental Engineering, Yale University, New Haven, Connecticut 06511, United States;* orcid.org/0000-0003-4544-6113

Tayler Hedtke − *Department of Chemical and Environmental Engineering, Yale University, New Haven, Connecticut 06511, United States*

Xiaoxiong Wang − *Department of Chemical and Environmental Engineering, Yale University, New Haven, Connecticut 06511, United States*

Myoung Won Chung − *School of Health and Environmental Science, Korea University, Seoul 02841, Republic of Korea*

Seunghyun Weon − *School of Health and Environmental Science, Korea University, Seoul 02841, Republic of Korea;* orcid.org/0000-0003-4529-8069

Eli Stavitski − *National Synchrotron Light Source II, Brookhaven National Laboratory, Upton, New York 11973, United States*

Complete contact information is available at: https://pubs.acs.org/10.1021/acs.est.1c06371

Notes

The authors declare no competing financial interest.

■ ACKNOWLEDGMENTS

This study was partly supported by the National Science Foundation (NSF) Nanosystems Engineering Research Center for Nanotechnology-Enabled Water Treatment (EEC-1449500) and NSF Division of Chemical, Bioengineering, Environmental, and Transport Systems (CBET) Grant #1955793. The authors would like to thank the Yale Institute for Nanoscience and Quantum Engineering (YINQE) for use of TEM, the Yale West Campus Materials Characterization Core (MCC) for use of XPS, SEM, XRD, Raman, and Chemical and Biophysical Instrumentation Center for use of FTIR and EPR. They are thankful to Professor John Fortner for the use of Zetasizer, and Dr. Wen Ma for the help with EPR measurements.

■ REFERENCES

(1) Lee, J.; Von Gunten, U.; Kim, J.-H. Persulfate-based advanced oxidation: critical assessment of opportunities and roadblocks. *Environ. Sci. Technol.* **2020**, *54*, 3064−3081.

(2) Zhang, S.; Sun, M.; Hedtke, T.; Deshmukh, A.; Zhou, X.; Weon, S.; Elimelech, M.; Kim, J.-H. Mechanism of heterogeneous Fenton reaction kinetics enhancement under nanoscale spatial confinement. *Environ. Sci. Technol.* **2020**, *54*, 10868−10875.

(3) Wu, H.; Xu, X.; Shi, L.; Yin, Y.; Zhang, L.-C.; Wu, Z.; Duan, X.; Wang, S.; Sun, H. Manganese oxide integrated catalytic ceramic membrane for degradation of organic pollutants using sulfate radicals. *Water Res.* **2019**, *167*, No. 115110.

(4) Xie, J.; Liao, Z.; Zhang, M.; Ni, L.; Qi, J.; Wang, C.; Sun, X.; Wang, L.; Wang, S.; Li, J. Sequential ultrafiltration-catalysis membrane for excellent removal of multiple pollutants in water. *Environ. Sci. Technol.* **2021**, *55*, 2652−2661.

(5) Han, G.; Chung, T.-S.; Weber, M.; Maletzko, C. Low-pressure nanofiltration hollow fiber membranes for effective fractionation of dyes and inorganic salts in textile wastewater. *Environ. Sci. Technol.* **2018**, *52*, 3676−3684.

(6) ElHadidy, A. M.; Peldszus, S.; Van Dyke, M. I. Development of a pore construction data analysis technique for investigating pore size distribution of ultrafiltration membranes by atomic force microscopy. *J. Membr. Sci.* **2013**, *429*, 373−383.

(7) Li, N.; Lu, X.; He, M.; Duan, X.; Yan, B.; Chen, G.; Wang, S. Catalytic membrane-based oxidation-filtration systems for organic wastewater purification: A review. *J. Hazard. Mater.* **2021**, No. 125478.

(8) Lee, B.-H.; Park, S.; Kim, M.; Sinha, A. K.; Lee, S. C.; Jung, E.; Chang, W. J.; Lee, K.-S.; Kim, J. H.; Cho, S.-P.; et al. Reversible and cooperative photoactivation of single-atom Cu/TiO2 photocatalysts. *Nat. Mater.* **2019**, *18*, 620−626.

(9) Yang, X.-F.; Wang, A.; Qiao, B.; Li, J.; Liu, J.; Zhang, T. Single-atom catalysts: a new frontier in heterogeneous catalysis. *Acc. Chem. Res.* **2013**, *46*, 1740−1748.

(10) Aliyev, E.; Filiz, V.; Khan, M. M.; Lee, Y. J.; Abetz, C.; Abetz, V. Structural characterization of graphene oxide: Surface functional groups and fractionated oxidative debris. *Nanomaterials* **2019**, *9*, No. 1180.

(11) Liu, Y.; Tang, N.; Wan, X.; Feng, Q.; Li, M.; Xu, Q.; Liu, F.; Du, Y. Realization of ferromagnetic graphene oxide with high magnetization by doping graphene oxide with nitrogen. *Sci. Rep.* **2013**, *3*, No. 2566.

(12) Willcox, J. A.; Kim, H. J. Molecular dynamics study of water flow across multiple layers of pristine, oxidized, and mixed regions of graphene oxide: effect of graphene oxide layer-to-layer distance. *J. Phys. Chem. C* **2017**, *121*, 23659−23668.

(13) Chen, F.; Wu, X.-L.; Yang, L.; Chen, C.; Lin, H.; Chen, J. Efficient degradation and mineralization of antibiotics via heterogeneous activation of peroxymonosulfate by using graphene supported single-atom Cu catalyst. *Chem. Eng. J.* **2020**, *394*, No. 124904.

(14) Li, J.; Zhao, S.; Zhang, L.; Jiang, S. P.; Yang, S. Z.; Wang, S.; Sun, H.; Johannessen, B.; Liu, S. Cobalt Single Atoms Embedded in Nitrogen-Doped Graphene for Selective Oxidation of Benzyl Alcohol by Activated Peroxymonosulfate. *Small* **2021**, *17*, No. 2004579.

(15) Li, X.; Huang, X.; Xi, S.; Miao, S.; Ding, J.; Cai, W.; Liu, S.; Yang, X.; Yang, H.; Gao, J.; et al. Single cobalt atoms anchored on porous N-doped graphene with dual reaction sites for efficient Fenton-like catalysis. *J. Am. Chem. Soc.* **2018**, *140*, 12469−12475.

(16) Long, Y.; Dai, J.; Zhao, S.; Su, Y.; Wang, Z.; Zhang, Z. Atomically Dispersed Cobalt Sites on Graphene as Efficient Periodate Activators for Selective Organic Pollutant Degradation. *Environ. Sci. Technol.* **2021**, *55*, 5357−5370.

(17) Chen, L.; Xing, K.; Shentu, Q.; Huang, Y.; Lv, W.; Yao, Y. Well-dispersed iron and nitrogen co-doped hollow carbon microsphere anchoring by g-C3N4 for efficient peroxymonosulfate activation. *Chemosphere* **2021**, No. 130911.

(18) Li, J.; Zhao, S.; Yang, S.-Z.; Wang, S.; Sun, H.; Johannessen, B.; Liu, S.; et al. Atomically dispersed cobalt on graphitic carbon nitride as a robust catalyst for selective oxidation of ethylbenzene by peroxymonosulfate. *J. Mater. Chem. A* **2021**, *9*, 3029−3035.

(19) Miao, W.; Liu, Y.; Wang, D.; Du, N.; Ye, Z.; Hou, Y.; Mao, S.; Ostrikov, K. K. The role of Fe-Nx single-atom catalytic sites in peroxymonosulfate activation: formation of surface-activated complex and non-radical pathways. *Chem. Eng. J.* **2021**, No. 130250.

(20) Qian, K.; Chen, H.; Li, W.; Ao, Z.; Wu, Y.-n.; Guan, X. Single-Atom Fe Catalyst Outperforms Its Homogeneous Counterpart for Activating Peroxymonosulfate to Achieve Effective Degradation of Organic Contaminants. *Environ. Sci. Technol.* **2021**, *55*, 7034−7043.

(21) Li, Y.; Yang, T.; Qiu, S.; Lin, W.; Yan, J.; Fan, S.; Zhou, Q. Uniform N-coordinated single-atomic iron sites dispersed in porous carbon framework to activate PMS for efficient BPA degradation via high-valent iron-oxo species. *Chem. Eng. J.* **2020**, *389*, No. 124382.

(22) Mi, X.; Wang, P.; Xu, S.; Su, L.; Zhong, H.; Wang, H.; Li, Y.; Zhan, S. Almost 100% peroxymonosulfate conversion to singlet oxygen on single-atom CoN2 + 2 sites. *Angew. Chem.* **2021**, *133*, 4638−4643.

(23) Yang, T.; Fan, S.; Li, Y.; Zhou, Q. Fe-N/C single-atom catalysts with high density of Fe-Nx sites toward peroxymonosulfate activation for high-efficient oxidation of bisphenol A: Electron-transfer mechanism. *Chem. Eng. J.* **2021**, *419*, No. 129590.
(24) Song, H.; Du, R.; Wang, Y.; Zu, D.; Zhou, R.; Cai, Y.; Wang, F.; Li, Z.; Shen, Y.; Li, C. Anchoring single atom cobalt on two-dimensional MXene for activation of peroxymonosulfate. *Appl. Catal., B* **2021**, *286*, No. 119898.
(25) Li, Z.; Li, K.; Ma, S.; Dang, B.; Li, Y.; Fu, H.; Du, J.; Meng, Q. Activation of peroxymonosulfate by iron-biochar composites: Comparison of nanoscale Fe with single-atom Fe. *J. Colloid Interface Sci.* **2021**, *582*, 598−609.
(26) Pan, J.; Gao, B.; Duan, P.; Guo, K.; Akram, M.; Xu, X.; Yue, Q.; Gao, Y. Improving peroxymonosulfate activation by copper ion-saturated adsorbent-based single atom catalysts for the degradation of organic contaminants: electron-transfer mechanism and the key role of Cu single atoms. *J. Mater. Chem. A* **2021**, *9*, 11604−11613.
(27) Huang, H.-H.; Joshi, R. K.; De Silva, K. K. H.; Badam, R.; Yoshimura, M. Fabrication of reduced graphene oxide membranes for water desalination. *J. Membr. Sci.* **2019**, *572*, 12−19.
(28) Pollitt, K. J. G.; Kim, J.-H.; Peccia, J.; Elimelech, M.; Zhang, Y.; Charkoftaki, G.; Hodges, B.; Zucker, I.; Huang, H.; Deziel, N. C.; et al. 1, 4-Dioxane as an emerging water contaminant: State of the science and evaluation of research needs. *Sci. Total Environ.* **2019**, *690*, 853−866.
(29) Adamson, D. T.; Piña, E. A.; Cartwright, A. E.; Rauch, S. R.; Anderson, R. H.; Mohr, T.; Connor, J. A. 1, 4-Dioxane drinking water occurrence data from the third unregulated contaminant monitoring rule. *Sci. Total Environ.* **2017**, *596*−*597*, 236−245.
(30) Abe, A. Distribution of 1, 4-dioxane in relation to possible sources in the water environment. *Sci. Total Environ.* **1999**, *227*, 41−47.
(31) Linares, R. V.; Yangali-Quintanilla, V.; Li, Z.; Amy, G. Rejection of micropollutants by clean and fouled forward osmosis membrane. *Water Res.* **2011**, *45*, 6737−6744.
(32) Schoonenberg Kegel, F.; Rietman, B.; Verliefde, A. Reverse osmosis followed by activated carbon filtration for efficient removal of organic micropollutants from river bank filtrate. *Water Sci. Technol.* **2010**, *61*, 2603−2610.
(33) Marcano, D. C.; Kosynkin, D. V.; Berlin, J. M.; Sinitskii, A.; Sun, Z.; Slesarev, A.; Alemany, L. B.; Lu, W.; Tour, J. M. Improved synthesis of graphene oxide. *ACS Nano* **2010**, *4*, 4806−4814.
(34) Lee, S.; Park, G.; Amy, G.; Hong, S.-K.; Moon, S.-H.; Lee, D.-H.; Cho, J. Determination of membrane pore size distribution using the fractional rejection of nonionic and charged macromolecules. *J. Membr. Sci.* **2002**, *201*, 191−201.
(35) Liang, C.; Huang, C.-F.; Mohanty, N.; Kurakalva, R. M. A rapid spectrophotometric determination of persulfate anion in ISCO. *Chemosphere* **2008**, *73*, 1540−1543.
(36) Gao, C.; Chen, S.; Wang, Y.; Wang, J.; Zheng, X.; Zhu, J.; Song, L.; Zhang, W.; Xiong, Y. Heterogeneous single-atom catalyst for visible-light-driven high-turnover CO2 reduction: the role of electron transfer. *Adv. Mater.* **2018**, *30*, No. 1704624.
(37) Tan, B. J.; Klabunde, K. J.; Tanaka, T.; Kanai, H.; Yoshida, S. An EXAFS study of cobalt-manganese/silica bimetallic solvated metal atom dispersed (SMAD) catalysts. *J. Am. Chem. Soc.* **1988**, *110*, 5951−5958.
(38) Koyano, G.; Watanabe, H.; Okuhara, T.; Misono, M. Structure and catalysis of cobalt oxide overlayers prepared on zirconia by low-temperature-plasma oxidation. *J. Chem. Soc., Faraday Trans.* **1996**, *92*, 3425−3430.
(39) Cao, L.; Luo, Q.; Liu, W.; Lin, Y.; Liu, X.; Cao, Y.; Zhang, W.; Wu, Y.; Yang, J.; Yao, T.; et al. Identification of single-atom active sites in carbon-based cobalt catalysts during electrocatalytic hydrogen evolution. *Nat. Catal.* **2019**, *2*, 134−141.
(40) Ban, F.; Majid, S. R.; Huang, N. M.; Lim, H. Graphene oxide and its electrochemical performance. *Int. J. Electrochem. Sci.* **2012**, *7*, 4345−4351.
(41) Chaiyakun, S.; Witit-Anun, N.; Nuntawong, N.; Chindaudom, P.; Oaew, S.; Kedkeaw, C.; Limsuwan, P.; et al. Preparation and characterization of graphene oxide nanosheets. *Procedia Eng.* **2012**, *32*, 759−764.
(42) Chen, J.; Gu, B.; LeBoeuf, E. J.; Pan, H.; Dai, S. Spectroscopic characterization of the structural and functional properties of natural organic matter fractions. *Chemosphere* **2002**, *48*, 59−68.
(43) Yang, E.; Ham, M.-H.; Park, H. B.; Kim, C.-M.; Song, J.-h.; Kim, I. S. Tunable semi-permeability of graphene-based membranes by adjusting reduction degree of laminar graphene oxide layer. *J. Membr. Sci.* **2018**, *547*, 73−79.
(44) Huh, S. H. *Physics and Applications of Graphene: Experiments*; InTech, 2011; pp 73−90.
(45) De Silva, K. K. H.; Huang, H.-H.; Yoshimura, M. Progress of reduction of graphene oxide by ascorbic acid. *Appl. Surf. Sci.* **2018**, *447*, 338−346.
(46) Zhang, J.; Yang, H.; Shen, G.; Cheng, P.; Zhang, J.; Guo, S. Reduction of graphene oxide via L-ascorbic acid. *Chem. Commun.* **2010**, *46*, 1112−1114.
(47) Delgado, J. A.; Claver, C.; Castillón, S.; Curulla-Ferre, D.; Ordomsky, V. V.; Godard, C. Fischer−Tropsch synthesis catalysed by small TiO2 supported cobalt nanoparticles prepared by sodium borohydride reduction. *Appl. Catal., A* **2016**, *513*, 39−46.
(48) Ni, Y.; Cao, X.; Wu, G.; Hu, G.; Yang, Z.; Wei, X. Preparation, characterization and property study of zinc oxide nanoparticles via a simple solution-combusting method. *Nanotechnology* **2007**, *18*, No. 155603.
(49) Zheng, S.; Tu, Q.; Urban, J. J.; Li, S.; Mi, B. Swelling of graphene oxide membranes in aqueous solution: characterization of interlayer spacing and insight into water transport mechanisms. *ACS Nano* **2017**, *11*, 6440−6450.
(50) Zhang, L.; Dai, F.; Yi, R.; He, Z.; Wang, Z.; Chen, J.; Liu, W.; Xu, J.; Chen, L. Effect of physical and chemical structures of graphene oxide on water permeation in graphene oxide membranes. *Appl. Surf. Sci.* **2020**, *520*, No. 146308.
(51) Zubir, N. A.; Yacou, C.; Motuzas, J.; Zhang, X.; da Costa, J. C. D. Structural and functional investigation of graphene oxide−Fe3O4 nanocomposites for the heterogeneous Fenton-like reaction. *Sci. Rep.* **2014**, *4*, No. 4594.
(52) Olmez-Hanci, T.; Arslan-Alaton, I.; Gurmen, S.; Gafarli, I.; Khoei, S.; Safaltin, S.; Ozcelik, D. Y. Oxidative degradation of Bisphenol A by carbocatalytic activation of persulfate and peroxymonosulfate with reduced graphene oxide. *J. Hazard. Mater.* **2018**, *360*, 141−149.
(53) Pei, S.; Cheng, H.-M. The reduction of graphene oxide. *Carbon* **2012**, *50*, 3210−3228.
(54) Feng, Y.; Ying, G.-G.; Yang, Z.; Shih, K.; Li, H.; Wu, D. Sulfate radical-induced destruction of emerging contaminants using traces of cobalt ions as catalysts. *Chemosphere* **2020**, *256*, No. 127061.
(55) Feng, Y.; Li, H.; Lin, L.; Kong, L.; Li, X.-y.; Wu, D.; Zhao, H.; Shih, K. Degradation of 1, 4-dioxane via controlled generation of radicals by pyrite-activated oxidants: synergistic effects, role of disulfides, and activation sites. *Chem. Eng. J.* **2018**, *336*, 416−426.
(56) Feng, Y.; Lee, P.-H.; Wu, D.; Shih, K. Surface-bound sulfate radical-dominated degradation of 1, 4-dioxane by alumina-supported palladium (Pd/Al2O3) catalyzed peroxymonosulfate. *Water Res.* **2017**, *120*, 12−21.
(57) Ouyang, D.; Chen, Y.; Yan, J.; Qian, L.; Han, L.; Chen, M. Activation mechanism of peroxymonosulfate by biochar for catalytic degradation of 1, 4-dioxane: Important role of biochar defect structures. *Chem. Eng. J.* **2019**, *370*, 614−624.
(58) Son, H.-S.; Choi, S.-B.; Khan, E.; Zoh, K.-D. Removal of 1, 4-dioxane from water using sonication: Effect of adding oxidants on the degradation kinetics. *Water Res.* **2006**, *40*, 692−698.
(59) Stefan, M. I.; Bolton, J. R. Mechanism of the degradation of 1, 4-dioxane in dilute aqueous solution using the UV/hydrogen peroxide process. *Environ. Sci. Technol.* **1998**, *32*, 1588−1595.
(60) Kang, Y.-G.; Yoon, H.; Lee, W.; Kim, E.-j.; Chang, Y.-S. Comparative study of peroxide oxidants activated by nZVI: Removal

https://doi.org/10.1021/acs.est.1c06371
Environ. Sci. Technol. 2022, 56, 1341−1351

of 1, 4-Dioxane and arsenic (III) in contaminated waters. *Chem. Eng. J.* **2018**, *334*, 2511−2519.
(61) Ji, Y.; Dong, C.; Kong, D.; Lu, J. New insights into atrazine degradation by cobalt catalyzed peroxymonosulfate oxidation: kinetics, reaction products and transformation mechanisms. *J. Hazard. Mater.* **2015**, *285*, 491−500.
(62) Lim, J.; Yang, Y.; Hoffmann, M. R. Activation of peroxymonosulfate by oxygen vacancies-enriched cobalt-doped black TiO2 nanotubes for the removal of organic pollutants. *Environ. Sci. Technol.* **2019**, *53*, 6972−6980.
(63) Spiro, M. The standard potential of the peroxosulphate/sulphate couple. *Electrochim. Acta* **1979**, *24*, 313−314.
(64) Chu, C.; Yang, J.; Zhou, X.; Huang, D.; Qi, H.; Weon, S.; Li, J.; Elimelech, M.; Wang, A.; Kim, J.-H. Cobalt Single Atoms on Tetrapyridomacrocyclic Support for Efficient Peroxymonosulfate Activation. *Environ. Sci. Technol.* **2020**, 1242−1250.
(65) Anipsitakis, G. P.; Dionysiou, D. D. Radical generation by the interaction of transition metals with common oxidants. *Environ. Sci. Technol.* **2004**, *38*, 3705−3712.
(66) Liang, C.; Su, H.-W. Identification of sulfate and hydroxyl radicals in thermally activated persulfate. *Ind. Eng. Chem. Res.* **2009**, *48*, 5558−5562.
(67) Huang, Z.; Bao, H.; Yao, Y.; Lu, W.; Chen, W. Novel green activation processes and mechanism of peroxymonosulfate based on supported cobalt phthalocyanine catalyst. *Appl. Catal., B* **2014**, *154*−*155*, 36−43.
(68) Wei, Z.; Villamena, F. A.; Weavers, L. K. Kinetics and mechanism of ultrasonic activation of persulfate: an in situ EPR spin trapping study. *Environ. Sci. Technol.* **2017**, *51*, 3410−3417.
(69) Chen, L.; Ding, D.; Liu, C.; Cai, H.; Qu, Y.; Yang, S.; Gao, Y.; Cai, T. Degradation of norfloxacin by CoFe2O4-GO composite coupled with peroxymonosulfate: a comparative study and mechanistic consideration. *Chem. Eng. J.* **2018**, *334*, 273−284.
(70) Cashman, M. A.; Kirschenbaum, L.; Holowachuk, J.; Boving, T. B. Identification of hydroxyl and sulfate free radicals involved in the reaction of 1, 4-dioxane with peroxone activated persulfate oxidant. *J. Hazard. Mater.* **2019**, *380*, No. 120875.
(71) Xu, H.; Jiang, N.; Wang, D.; Wang, L.; Song, Y.; Chen, Z.; Ma, J.; Zhang, T. Improving PMS oxidation of organic pollutants by single cobalt atom catalyst through hybrid radical and non-radical pathways. *Appl. Catal., B* **2020**, *263*, No. 118350.
(72) Qin, W.; Fang, G.; Wang, Y.; Zhou, D. Mechanistic understanding of polychlorinated biphenyls degradation by peroxymonosulfate activated with CuFe2O4 nanoparticles: Key role of superoxide radicals. *Chem. Eng. J.* **2018**, *348*, 526−534.
(73) Wardman, P. Reduction potentials of one-electron couples involving free radicals in aqueous solution. *J. Phys. Chem. Ref. Data* **1989**, *18*, 1637−1755.
(74) Qi, Y.; Li, J.; Zhang, Y.; Cao, Q.; Si, Y.; Wu, Z.; Akram, M.; Xu, X. Novel lignin-based single atom catalysts as peroxymonosulfate activator for pollutants degradation: Role of single cobalt and electron transfer pathway. *Appl. Catal., B* **2021**, *286*, No. 119910.
(75) Fei, H.; Dong, J.; Chen, D.; Hu, T.; Duan, X.; Shakir, I.; Huang, Y.; Duan, X. Single atom electrocatalysts supported on graphene or graphene-like carbons. *Chem. Soc. Rev.* **2019**, *48*, 5207−5241.
(76) Zhang, S.; Hedtke, T.; Zhou, X.; Elimelech, M.; Kim, J.-H. Environmental Applications of Engineered Materials with Nanoconfinement. *ACS EST Eng.* **2021**, *1*, 706−724.
(77) Zhang, S.; Hedtke, T.; Zhu, Q.; Sun, M.; Weon, S.; Zhao, Y.; Stavitski, E.; Elimelech, M.; Kim, J.-H. Membrane-Confined Iron Oxychloride Nanocatalysts for Highly Efficient Heterogeneous Fenton Water Treatment. *Environ. Sci. Technol.* **2021**, *55*, 9266−9275.
(78) Li, W.; Patton, S.; Gleason, J. M.; Mezyk, S. P.; Ishida, K. P.; Liu, H. UV photolysis of chloramine and persulfate for 1, 4-dioxane removal in reverse-osmosis permeate for potable water reuse. *Environ. Sci. Technol.* **2018**, *52*, 6417−6425.
(79) Rodrigues, A.; Brito, A.; Janknecht, P.; Proença, M. F.; Nogueira, R. Quantification of humic acids in surface water: effects of divalent cations, pH, and filtration. *J. Environ. Monit.* **2009**, *11*, 377−382.
(80) Appiani, E.; Page, S. E.; McNeill, K. On the use of hydroxyl radical kinetics to assess the number-average molecular weight of dissolved organic matter. *Environ. Sci. Technol.* **2014**, *48*, 11794−11802.
(81) Zhang, S.; Rouge, V.; Gutierrez, L.; Croue, J.-P. Reactivity of chromophoric dissolved organic matter (CDOM) to sulfate radicals: Reaction kinetics and structural transformation. *Water Res.* **2019**, *163*, No. 114846.
(82) Iskander, S. M.; Zeng, T.; Smiley, E.; Bolyard, S. C.; Novak, J. T.; He, Z. Formation of disinfection byproducts during Fenton's oxidation of chloride-rich landfill leachate. *J. Hazard. Mater.* **2020**, *382*, No. 121213.
(83) Aiken, G. R.; Hsu-Kim, H.; Ryan, J. N. Influence of dissolved organic matter on the environmental fate of metals, nanoparticles, and colloids. *Environ. Sci. Technol.* **2011**, *45*, 3196−3201.
(84) Wu, X.; Bowers, B.; Kim, D.; Lee, B.; Jun, Y.-S. Dissolved organic matter affects arsenic mobility and iron (III)(hydr) oxide formation: implications for managed aquifer recharge. *Environ. Sci. Technol.* **2019**, *53*, 14357−14367.
(85) Hartono, T.; Wang, S.; Ma, Q.; Zhu, Z. Layer structured graphite oxide as a novel adsorbent for humic acid removal from aqueous solution. *J. Colloid Interface Sci.* **2009**, *333*, 114−119.
(86) Neta, P.; Huie, R. E.; Ross, A. B. Rate constants for reactions of inorganic radicals in aqueous solution. *J. Phys. Chem. Ref. Data* **1988**, *17*, 1027−1284.

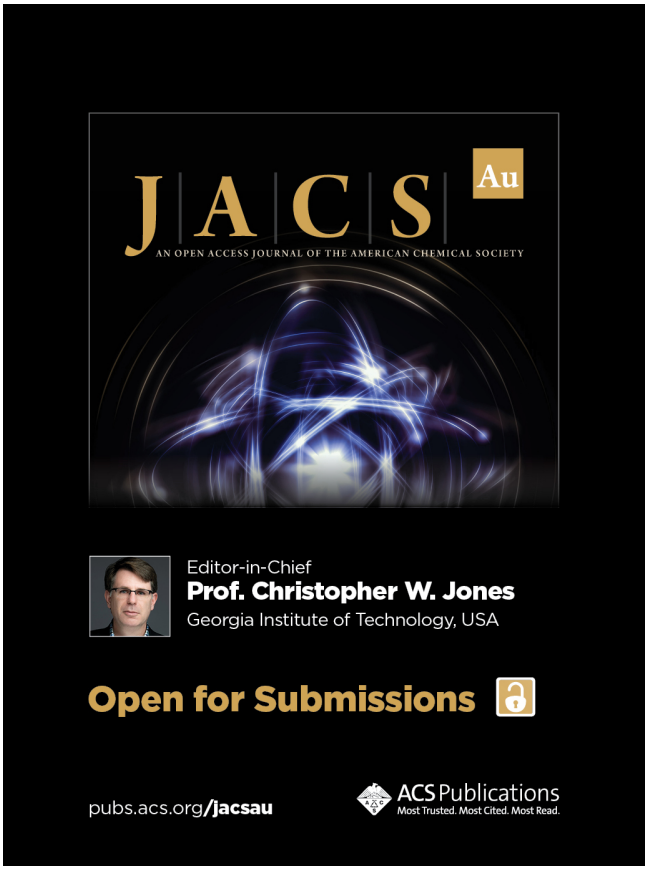

https://doi.org/10.1021/acs.est.1c06371
Environ. Sci. Technol. 2022, 56, 1341−1351